Effects of Compton cooling on the hydrodynamic and the spectral properties of a two-component accretion flow around a black hole

Himadri Ghosh,[1]★ Sudip K. Garain,[1]★ Kinsuk Giri[1]★ and Sandip K. Chakrabarti[1,2]★

[1]*S. N. Bose National Centre for Basic Sciences, Salt Lake, Kolkata 700098, India*
[2]*Indian Centre for Space Physics, Chalantika 43, Garia Station Road, Kolkata 700084, India*

ABSTRACT

We carry out a time-dependent numerical simulation where both the hydrodynamics and the radiative transfer are coupled together. We consider a two-component accretion flow in which the Keplerian disc is immersed inside an accreting low angular momentum flow (halo) around a black hole. The injected soft photons from the Keplerian disc are reprocessed by the electrons in the halo. We show that in presence of an axisymmetric soft-photon source the spherically symmetric Bondi flow loses its symmetry and becomes axisymmetric. The low angular momentum flow was observed to slow down close to the axis and formed a centrifugal barrier which added new features into the spectrum. Using the Monte Carlo method, we generated the radiated spectra as functions of the accretion rates. We find that the transitions from a hard state to a soft state is determined by the mass accretion rates of the disc and the halo. We separate out the signature of the bulk motion Comptonization and discuss its significance. We study how the net spectrum is contributed by photons suffering different number of scatterings and spending different amounts of time inside the Compton cloud. We study the directional dependence of the emitted spectrum as well.

Key words: accretion, accretion discs – black hole physics – hydrodynamics – radiation mechanisms: general – radiative transfer – methods: numerical.

1 INTRODUCTION

The spectral and timing properties of a black hole candidate give away the most vital clues to the understanding of the nature of the invisible central object. The spectrum of radiation, particularly in high energies, gives information about the thermodynamic properties of matter accreting on to a black hole. The timing properties give information about how these thermodynamic properties are changing with time. The thermodynamic properties such as the mass density, temperature, etc. and the dynamic properties such as the velocity components are the solutions of the governing equations. Thus, a thorough knowledge of the spectral and timing properties are essential (e.g. Chakrabarti 1996).

There are several papers in the literature which have devoted themselves to study the spectral and timing properties of the accretion flows around black holes. Sunyaev & Titarchuk (1980) suggested that the explanation of the emitted spectrum requires the presence of a Comptonizing hot electron plasma along with the standard disc of Shakura & Sunyaev (1973). There are several models in the literature, such as the hot corona on a Keplerian disc (Haardt & Maraschi 1993), unstable inner edge of the standard disc

(Kobayashi et al. 2003), hybrid EQPAIR model (Coppi 1992) which uses both the thermal and non-thermal electrons which empirically describe the nature of the possible Compton cloud. Other models include those of Wandel & Liang (1991), Janiuk & Czerny (2000), Merloni & Fabian (2001) and Zdziarski et al. (2003). In the so-called two-component advective flow model of Chakrabarti & Titarchuk (1995), which is based on shock solutions in a sub-Keplerian flow (Chakrabarti 1989), it was shown that the spectral properties are direct consequences of variation of accretion rates of the Keplerian (disc) and sub-Keplerian (halo) components. Subsequently, efforts were made to explain the timing properties. An important step in this direction is the theoretical work of Titarchuk & Lyubarskii (1995) and Lyubarskii (1997) who showed the influence of noise and turbulences on the power density spectrum. Meanwhile, almost at the same time, Molteni, Sponholz & Chakrabarti (1996) pointed out that the resonance effects between the cooling time-scale and the infall time-scale cause the Chakrabarti shocks (C-shocks) to oscillate and cause the most important feature of the power density spectrum, namely the quasi-periodic oscillations (QPOs). Molteni, Toth & Kuznetsov (1999) showed that these C-shocks are actually stable even when azimuthal perturbations are given, though a vortex was shown to rotate anchoring the shocks, causing further enhancements in QPO power densities. This was further expanded by Chakrabarti, Acharyya & Molteni (2004) who relaxed the constraints on the equatorial symmetry and found that these shocks are

★E-mail: himadri@bose.res.in (HG); sudip@bose.res.in (SKG); kinsuk@bose.res.in (KG); chakraba@bose.res.in (SKC)

prone to both vertical and radial oscillations of similar frequencies. Thus it is generally established that the sub-Keplerian flows are responsible for both the spectral and timing properties of the black hole candidates. This has been corroborated by several observations (Soria et al. 2001; Smith, Heindl & Swank 2002; Wu et al. 2002; Pottschmidt et al. 2006; Dutta & Chakrabarti 2010).

Given that the two-component flows have been found to be useful to understand the spectral and timing properties, it will be important to carry out the numerical simulations of radiative flows around black holes which also include C-shocks. So far, however, only bremsstrahlung or pseudo-Compton cooling have been added into the time-dependent flows (Molteni et al. 1996; Chakrabarti et al. 2004; Proga 2007; Proga, Ostriker & Kurosawa 2008). Inclusion of the full-fledged Comptonization is prohibitively complex since the Comptonization efficiency depends on temperature and optical depth of the surrounding flow, and this would depend on directions and time as well. In the present paper, we make the first attempt to incorporate the time-dependent simulation result which includes both hydrodynamics and radiative transfer. We use the low angular halo along with a Keplerian disc. We find how the Comptonization affects the temperature distribution of the flow and how this in turn affects the dynamics of the flow as well. So far, our solutions have been steady. We obtain the outgoing spectrum of radiation as well.

In the next section, we discuss the geometry of the soft photon source and the Compton cloud in our Monte Carlo simulations. The variation of the thermodynamic quantities and other vital parameters are obtained inside the Keplerian disc and the Compton cloud which are required for the Monte Carlo simulations. In Section 3 we describe the simulation procedure, and in Section 4 we present the results of our simulations. Finally, in Section 5 we make concluding remarks.

2 GEOMETRY OF THE ELECTRON CLOUD AND THE SOFT-PHOTON SOURCE

In Figs 1(a) and (b), we present cartoon diagrams of our simulation set-up for (a) spherical Compton cloud (halo) with zero angular momentum (specific angular momentum, i.e. angular momentum per unit mass, $\lambda = 0$) and (b) rotating Compton cloud (halo) with a specific angular momentum $\lambda = 1$. In the first case (a), we have the electron cloud within a sphere of radius $R_{in} = 200r_g$, the Keplerian disc resides at the equatorial plane. The outer edge of this disc is located at $R_{out} = 300r_g$, and it extends up to the marginally stable orbit $R_{ms} = 3r_g$. At the centre of the sphere, a black hole of mass $10\,M_\odot$ is located. The spherical matter is injected into the sphere from the radius R_{in}. It intercepts the soft photons emerging out of

the Keplerian disc and reprocesses them via Compton or inverse-Compton scattering. An injected photon may undergo a single, multiple or no scattering at all with the hot electrons in between its emergence from the Keplerian disc and its escape from the halo. The photons which enter the black holes are absorbed. In the second case (b), due to the presence of the angular momentum of the flow, the spherical symmetry of the flow is lost. The other parameters of the Keplerian disc and the halo remain the same as in case (a).

2.1 Distribution of temperature and density inside the Compton cloud

A realistic accretion disc is expected to be three-dimensional. Assuming axisymmetry, we have calculated the flow dynamics using a finite difference method which uses the principle of total variation diminishing (TVD) to carry out hydrodynamic simulations (see Ryu, Chakrabarti & Molteni 1997, and references therein; Giri et al. 2010). At each time-step, we carry out Monte Carlo simulation to obtain the cooling/heating due to Comptonization. We incorporate the cooling/heating of each grid while executing the next time-step of hydrodynamic simulation. The numerical calculation for the two-dimensional flow has been carried out with 900×900 cells in a $200r_g \times 200r_g$ box. We chose the units in a way that the outer boundary (R_{in}) is chosen to be unity and the matter density is normalized to become unity. We assume the black hole to be non-rotating, and we use the pseudo-Newtonian potential $-1/2(r-1)$ (Paczyński & Wiita 1980) to calculate the flow geometry around a black hole (here r is in the unit of Schwarzschild radius $r_g = 2GM_{bh}/c^2$). Velocities and angular momenta are measured in units of c, the velocity of light, and r_gc, respectively. In Figs 2(a) and (b), we show the snapshots of the density and temperature (in keV) profiles obtained in a steady state purely from our hydrodynamic simulation. The density contour levels are drawn for 0.65–1.01 (levels increasing by a factor of 1.05) and 1.01–66.93 (successive level ratio is 1.1). The temperature contour levels are drawn for 16.88–107.8 keV (successive level ratio is 1.05).

2.2 Properties of the Keplerian disc

The soft photons are produced from a Keplerian disc whose inner edge has been kept fixed at the marginally stable orbit R_{ms}, while the outer edge is located at R_{out} (= assumed to be at $300r_g$ in this paper). The source of the soft photons has a multicolour blackbody spectrum coming from a standard (Shakura & Sunyaev 1973, hereafter SS73) disc. We assume the disc to be optically thick and the opacity due to free–free absorption is more important than the opacity due to
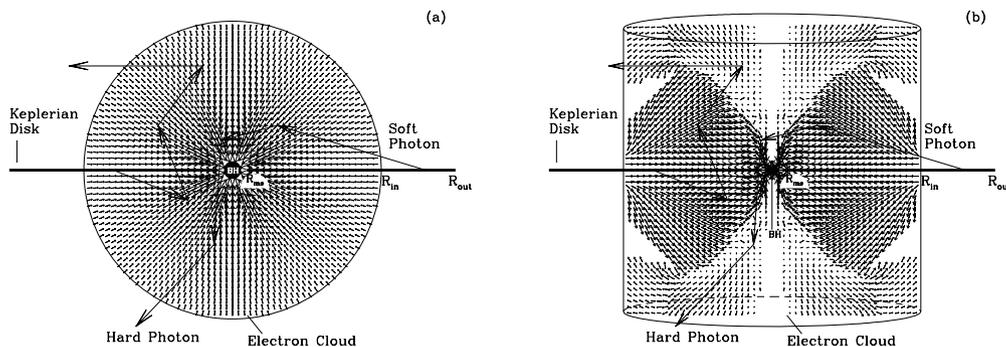
Figure 1. Schematic diagram of the geometry of our Monte Carlo simulations for (a) $\lambda = 0$ and for (b) $\lambda = 1$. Zigzag trajectories and velocity vectors are typical paths followed by the photons and the velocity vectors of the infalling matter inside the cloud.
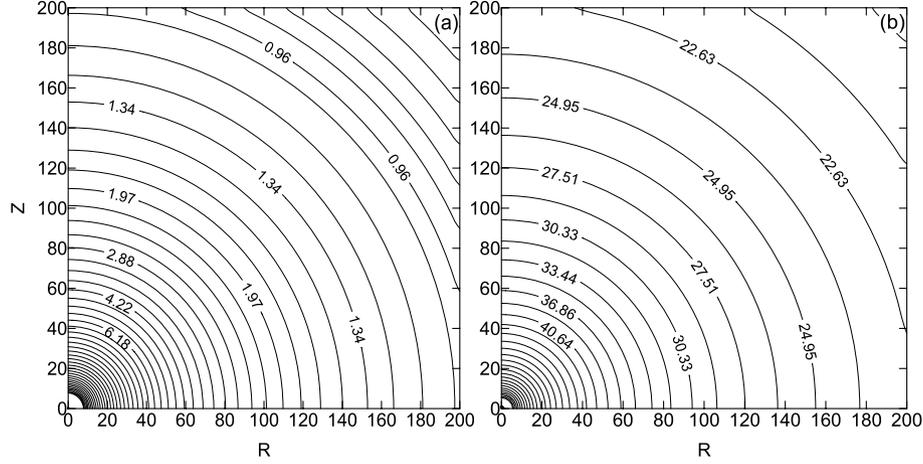
Figure 2. Density (a) and temperature (b) contours inside the spherical halo in the absence of Compton cooling. Here, densities are in normalized unit and temperatures are in keV. $\lambda = 0$ is chosen. See text for details.

scattering. The emission is blackbody type with the local surface temperature (SS73):

$$T(r) \approx 5 \times 10^7 (M_{bh})^{-1/2} (\dot{M}_{d17})^{1/4} (2r)^{-3/4} \left[1 - \sqrt{\frac{3}{r}} \right]^{1/4} \text{ K,} \quad (1)$$

The total number of photons emitted from the disc surface is obtained by integrating over all frequencies (ν) and is given by

$$n_\gamma(r) = \left[16\pi \left(\frac{k_b}{hc} \right)^3 \times 1.202057 \right] [T(r)]^3. \quad (2)$$

The disc between radius r to $r + \delta r$ injects $dN(r)$ number of soft photons:

$$dN(r) = 4\pi r \delta r H(r) n_\gamma(r), \quad (3)$$

where $H(r)$ is the half-height of the disc given by

$$H(r) = 10^5 \dot{M}_{d17} \left[1 - \sqrt{\frac{3}{r}} \right] \text{ cm.} \quad (4)$$

In the Monte Carlo simulation, we incorporated the directional effects of photons coming out of the Keplerian disc with the maximum number of photons emitted in the z-direction and minimum number of photons are generated along the plane of the disc. Thus, in the absence of photon bending effects, the disc is invisible as seen edge-on. The position of each emerging photon is randomized using the distribution function (equation 3). In the above equations, the mass of the black hole M_{bh} is measured in units of the mass of the Sun ($M_\odot$), the disc accretion rate $\dot{M}_{d17}$ is in units of 10^{17} gm s^{-1}. We chose $M_{bh} = 10$ in the rest of the paper.

3 SIMULATION PROCEDURE

In a given run, we assume a Keplerian disc rate ($\dot{m}_d$) and a sub-Keplerian halo rate ($\dot{m}_h$). The specific energy (ϵ) of the halo provides the hydrodynamic (e.g. number density of the electrons and the velocity distribution) and the thermal properties of matter. Since we chose the Paczyński & Wiita (1980) potential, the radial velocity is not exactly unity at $r = 1$, the horizon. It becomes unity just outside. In order not to overestimate the effects of bulk motion Comptonization (Chakrabarti & Titarchuk 1995) which is due to the momentum transfer of the moving electrons to the horizon, we kept the highest velocity to be 1. We use the absorbing boundary

condition at $r = 1.5$ ($\lambda = 0$ case) and $r = 2.5$ ($\lambda = 1$ case). These simplifying assumptions do not affect our conclusions, especially because we are studying inviscid flow and the specific angular momentum is constant. Photons are generated from the Keplerian disc as mentioned before and may be intercepted by the sub-Keplerian halo [sphere in Fig. 1(a) and cylinder in Fig. 1(b)].

To begin the Monte Carlo code, we randomly generated soft photons from the Keplerian disc. The energy of the soft photon at radiation temperature $T(r)$ is calculated using the Planck's distribution formula, where the number density of the photons [$n_\gamma(E)$] having an energy E is expressed by

$$n_\gamma(E) = \frac{1}{2\zeta(3)} b^3 E^2 (e^{bE} - 1)^{-1}, \quad (5)$$

where $b = 1/kT(r)$ and $\zeta(3) = \sum_1^\infty l^{-3} = 1.202$, the Riemann zeta function.

Using another set of random numbers we obtained the direction of the injected photon, and with yet another random number we obtained a target optical depth τ_c at which the scattering takes place. The photon was followed within the electron cloud till the optical depth (τ) reached τ_c. The increase in optical depth ($d\tau$) during its travelling of a path of length dl inside the electron cloud is given by $d\tau = \rho_n \sigma \, dl$, where ρ_n is the electron number density.

The total scattering cross-section σ is given by Klein–Nishina formula:

$$\sigma = \frac{2\pi r_e^2}{x} \left[\left(1 - \frac{4}{x} - \frac{8}{x^2} \right) \ln(1 + x) + \frac{1}{2} + \frac{8}{x} - \frac{1}{2(1+x)^2} \right], \quad (6)$$

where x is given by

$$x = \frac{2E}{mc^2} \gamma \left(1 - \mu \frac{v}{c} \right), \quad (7)$$

$r_e = e^2/mc^2$ is the classical electron radius and m is the mass of the electron.

We have assumed here that a photon of energy E and momentum $\frac{E}{c} \widehat{\Omega}$ is scattered by an electron of energy γmc^2 and momentum $p = \gamma m v$, with $\gamma = (1 - \frac{v^2}{c^2})^{-1/2}$ and $\mu = \widehat{\Omega} \cdot \hat{v}$. At this point, a scattering is allowed to take place. The photon selects an electron and the energy exchange is computed using the Compton or inverse-Compton scattering formula. The electrons are assumed to obey relativistic Maxwell distribution inside the Compton cloud. The number $dN(p)$ of Maxwellian electrons having momentum between

p to $p + dp$ is expressed by

$$dN(\boldsymbol{p}) \propto \exp\left[-(p^2c^2 + m^2c^4)^{1/2}/kT_e\right] d\boldsymbol{p}. \quad (8)$$

We take a steady-state flow profile from a hydrodynamics code to start the Monte Carlo simulation. When a photon interacts with an electron via Compton or inverse-Compton scattering, it loses or gains some energy (ΔE). At each grid point, we compute ΔE. We update the energy of the flow at this grid by this amount and continue the hydrodynamic code with this modified energy. This, in turn, modify the hydrodynamic profile. Thus the Monte Carlo code for radiative transport and numerical code are coupled together. In case the final state is steady, the temperature of the cloud would be reduced progressively to a steady value from the initial state where no cooling was assumed. If the final state is oscillatory, the solution would settle into a state with Comptonization.

3.1 Details of the coupling procedure

Once a steady state is achieved in the non-radiative hydrodynamic code, we compute the spectrum using the Monte Carlo code. This is the spectrum in the first approximation. To include cooling in the coupled code, we follow the following steps. (i) We calculate the velocity, density and temperature profiles of the electron cloud from the output of the hydrodynamic code. (ii) Using the Monte Carlo code we calculate the spectrum. (iii) Electrons are cooled (heated up) by the inverse-Compton (Compton) scattering. We calculate the amount of heat loss (gain) by the electrons and its new temperature and energy distributions and (iv) taking the new temperature and energy profiles as initial condition, we run the hydrodynamic code for a period of time. Subsequently, we repeat the steps (i)–(iv). In this way, we get an opportunity to see how the spectrum is modified as the iterations proceed. The iterations stop when two successive steps produce virtually the same temperature profile and the emitted spectrum.

3.1.1 Calculation of energy reduction using Monte Carlo code

For Monte Carlo simulation, we divide the Keplerian disc into different annuli of width $D(r) = 0.5$. Each annulus is characterized by its central temperature $T(r)$. The total number of photons emitted from the disc surface of each annulus can be calculated using equation (3). This total number comes out to be $\sim 10^{39-40}$ for $\dot{m}_d = 1.0$. In reality, one cannot inject this much number of photons in Monte Carlo simulation because of the limitation of computation time. Therefore, we replace this large number of photons by a low number of bundles, say, $N_{comp}(r) \sim 10^7$ and calculate a weightage factor:

$$f_W = \frac{dN(r)}{N_{comp}(r)}.$$

Clearly, from each annulus, the number of photons in a bundle will vary. This is computed exactly and used to compute the change of energy due to Comptonization. When this injected photon is inverse-Comptonized (or Comptonized) by an electron in a volume element of size dV, we assume that f_W number of photons has suffered similar scattering with the electrons inside the volume element dV. If the energy loss (gain) per electron in this scattering is ΔE, we multiply this amount by f_W and distribute this loss (gain) among all the electrons inside that particular volume element. This is continued for all the 10^7 bundles of photons and the revised energy distribution is obtained.

3.1.2 Computation of the temperature distribution after cooling

Since the hydrogen plasma considered here is ultrarelativistic ($\gamma = 4/3$ throughout the hydrodynamic simulation), thermal energy per particle is $3k_B T$ where k_B is Boltzmann constant, T is the temperature of the particle. The electrons are cooled by the inverse-Comptonization of the soft photons emitted from the Keplerian disc. The protons are cooled because of the Coulomb coupling with the electrons. Total number of electrons inside any box with the centre at location (ir, iz) is given by

$$dN_e(ir, iz) = 4\pi r n_e(ir, iz) dr dz, \quad (9)$$

where $n_e(ir, iz)$ is the electron number density at (ir, iz) location, and dr and dz represent the grid size along r- and z-directions, respectively. Therefore the total thermal energy in any box is given by $3k_B T(ir, iz) dN_e(ir, iz) = 12\pi r k_B T(ir, iz) n_e(ir, iz) dr dz$, where $T(ir, iz)$ is the temperature at (ir, iz) grid. We calculate the total energy loss (gain) ΔE of electrons inside the box according to what is presented above and subtract that amount to get the new temperature of the electrons inside that box as

$$k_B T_{new}(ir, iz) = k_B T_{old}(ir, iz) - \frac{\Delta E}{3 dN_e(ir, iz)}. \quad (10)$$

3.2 Details of the hydrodynamic simulation code

As mentioned above, after every spell of cooling by the Monte Carlo code for a very short time-step, the hydrodynamic code is run without assuming cooling. This procedure is repeated. While running the hydrodynamic code the following process is followed.

To model the initial injection of matter, we consider an axisymmetric flow of gas in the pseudo-Newtonian gravitational field of a black hole of mass M_{bh} located at the centre in the cylindrical coordinates $[R, \theta, z]$. We assume that at infinity, the gas pressure is negligible and the energy per unit mass vanishes. We also assume that the gravitational field of the black hole can be described by Paczyński & Wiita (1980):

$$\phi(r) = -\frac{GM_{bh}}{(r - r_g)},$$

where $r = \sqrt{R^2 + z^2}$, and the Schwarzschild radius is given by

$$r_g = 2GM_{bh}/c^2.$$

We also assume a polytropic equation of state for the accreting (or outflowing) matter, $P = K\rho^\gamma$, where P and ρ are the isotropic pressure and the matter density respectively, γ is the adiabatic index (assumed to be constant throughout the flow, and is related to the polytropic index n by $\gamma = 1 + 1/n$) and K is related to the specific entropy of the flow s. The details of the code is described in Ryu et al. (1997) and in Giri et al. (2010).

Our computational box occupies one quadrant of the R–z plane with $0 \le R \le 200$ and $0 \le z \le 200$. The incoming gas enters the box through the outer boundary, located at $R_{in} = 200$. We have chosen the density of the incoming gas $\rho_{in} = 1$ for convenience, since, in the absence of self-gravity and cooling, the density is scaled out, rendering the simulation results valid for any accretion rate. As we are considering only energy flows while keeping the boundary of the numerical grid at a finite distance, we need the sound speed a (i.e. temperature) of the flow and the incoming velocity at the boundary points. For the spherical flow with zero angular momentum (Bondi flow), we have taken the boundary values from standard pseudo-Bondi solution. We injected the matter from both the outer boundary

Table 1. Parameters used for the simulations and a summary of results.

Case	λ	ϵ	$\dot{m}_d$	$\dot{m}_h$	N_{inj}	N_{sc}	N_{unsc}	N_{bh} (per cent)	p (per cent)	t_0 (s)	α
1a	0	22E−4	1	1	4.3E+40	8.7E+39	3.5E+40	0.119	20.030	228.3	1.15, 0.99
1b	0	22E−4	2	1	1.5E+41	2.9E+40	1.2E+41	0.120	20.023	63.6	1.30, 1.0
1c	0	22E−4	5	1	7.3E+41	1.5E+41	5.9E+41	0.121	19.942	12.4	1.40, 0.96
1d	0	22E−4	10	1	2.5E+42	5.0E+41	2.0E+42	0.121	19.816	4.2	1.65, 0.90
1e	0	22E−4	1	0.5	4.3E+40	4.7E+39	3.9E+40	0.070	10.886	380.0	1.57
1f	0	22E−4	1	2	4.3E+40	1.5E+40	2.8E+40	0.230	34.324	118.9	1.1
1g	0	22E−4	1	5	4.3E+40	2.6E+40	1.8E+40	0.502	59.012	48.0	0.7
1h	0	22E−4	1	10	4.3E+40	3.3E+40	1.1E+40	0.699	75.523	35.1	0.45
2a	1	3E−4	1	1	6.3E+40	1.2E+40	5.1E+40	0.285	19.199	79.7	0.88
2b	1	3E−4	2	1	2.1E+41	4.1E+40	1.7E+41	0.283	19.278	21.9	0.94
2c	1	3E−4	5	1	1.0E+42	1.9E+41	8.1E+41	0.283	19.205	4.3	1.03
2d	1	3E−4	10	1	3.6E+42	6.9E+41	2.9E+42	0.289	18.941	1.4	1.17
2e	1	3E−4	10	0.5	3.6E+42	3.9E+41	3.2E+42	0.190	10.768	1.9	1.37
2f	1	3E−4	10	1.5	3.6E+42	9.3E+41	2.7E+42	0.372	25.492	1.1	1.01
2g	1	3E−4	10	2	3.6E+42	1.1E+42	2.5E+42	0.443	30.758	0.9	0.95
2h	1	3E−4	10	5	3.6E+42	1.8E+42	1.7E+42	0.690	51.073	0.7	0.59

of R and z coordinate. In order to mimic the horizon of the black hole at the Schwarzschild radius, we placed an absorbing inner boundary at $r = 1.5r_g$, inside which all material is completely absorbed into the black hole. For the background matter (required to avoid division by zero) we used a stationary gas with density $\rho_{bg} = 10^{-6}$ and sound speed (or temperature) the same as that of the incoming gas. Hence the incoming matter has a pressure 10^6 times larger than that of the background matter. All the calculations were performed with 900×900 cells, so each grid has a size of 0.22 in units of the Schwarzschild radius.

All the simulations are carried out assuming a stellar mass black hole ($M = 10\,M_\odot$). The procedures remain equally valid for massive/supermassive black holes. We carry out the simulations till several thousands of dynamical time-scales are passed. In reality, this corresponds to a few seconds in physical units.

4 RESULTS AND DISCUSSIONS

In Table 1, we summarize all the cases for which the simulations have been presented in this paper. In column 1, various cases are marked. Columns 2 and 3 give the angular momentum (λ) and the specific energy (ϵ) of the flow. The Keplerian disc rate ($\dot{m}_d$) and the sub-Keplerian halo rate ($\dot{m}_h$) are listed in columns 4 and 5. The number of soft photons, injected from the Keplerian disc (N_{inj}) for various disc rates can be found in column 6. Column 7 lists the number of photons (N_{sc}) that have suffered at least one scattering inside the electron cloud. The number of photons (N_{unsc}), escaped from the cloud without any scattering are listed in column 8. Columns 9 and 10 give the percentages of injected photons that have entered into the black hole (N_{bh}) and suffered scattering ($p = N_{sc}/N_{inj}$), respectively. The cooling time (t_0) of the system is defined as the expected time for the system to lose all its thermal energy with the particular flow parameters (namely, $\dot{m}_d$ and $\dot{m}_h$). We calculate $t_0 = E/\dot{E}$ in each time-step, where E is the total energy content of the system and $\dot{E}$ is the energy gain or loss by the system in that particular time-step. We present the energy spectral index α [$I(E) \sim E^{-\alpha}$] obtained from our simulations in the last column.

4.1 Compton cloud with no angular momentum

First we discuss the results corresponding to the cases 1(a–d) of Table 1. In Figs 3(a–d) we present the changes in density distribution

as the disc accretion rates are changed: $\dot{m}_d =$ (a) 1, (b) 2, (c) 5 and (d) 10, respectively. We note that as the accretion rate of the disc is enhanced, the density distribution loses its spherical symmetry. In particular, the density at a given radius is enhanced in a conical region along the axis. This is due to the cooling of the matter by Compton scattering. To show this, in Figs 4(a–d) we show the contours of constant temperatures (marked on curves) of the same four cases. We note that the temperature is reduced along the axis (where the optical depth as seen by the soft photons from the Keplerian disc is higher) drastically after repeated Compton scattering.

In Figs 5(a–d), we show the hydrodynamic and radiative properties. In Fig. 5(a), we show the sonic surfaces. The lowermost curve corresponds to theoretical solution for an adiabatic flow (e.g. Chakrabarti 1990). Other curves from the bottom to the top are the iterative solutions for the case 1d mentioned above. As the disc rate is increased, the cooling increases, and consequently, the Mach number increases along the axis. Of course, there are other effects: the cooling causes the density to go up to remain in pressure equilibrium. In Fig. 5(b), the Mach number variation is shown. The lowermost curve (marked 1) is from the theoretical consideration. Plots 2–4 are the variation of Mach number with radial distance along the equatorial plane, along the diagonal and along the vertical axis, respectively. In Fig. 5(c), the average temperature of the spherical halo is plotted as a function of the iteration time until almost steady state is reached. The cases are marked on the curves. We note that as the injection of soft photons increases, the average temperature of the halo decreases drastically. In Fig. 5(d), we have plotted the energy dependence of the photon intensity. We find that, as we increase the disc rate and keeping the halo rate fixed, the number of photons coming out of the cloud in a particular energy bin increases and the spectrum becomes softer. This is also clear from Table 1: N_{inj} increases with $\dot{m}_d$, thereby increasing α. We find the signature of double slope in these cases. As the disc rate increases, the second slope becomes steeper. This second slope is the signature of bulk motion Comptonization. As $\dot{m}_d$ increases, the cloud becomes cooler [plot 5(c)] and the power-law tail due to the bulk motion Comptonization (Chakrabarti & Titarchuk 1995) becomes prominent.

In Fig. 6(a), we show the variation of the energy spectrum with the increase of the halo accretion rate, keeping the disc rate ($\dot{m}_d = 1$) and angular momentum of the flow ($\lambda = 0$) fixed. The injected
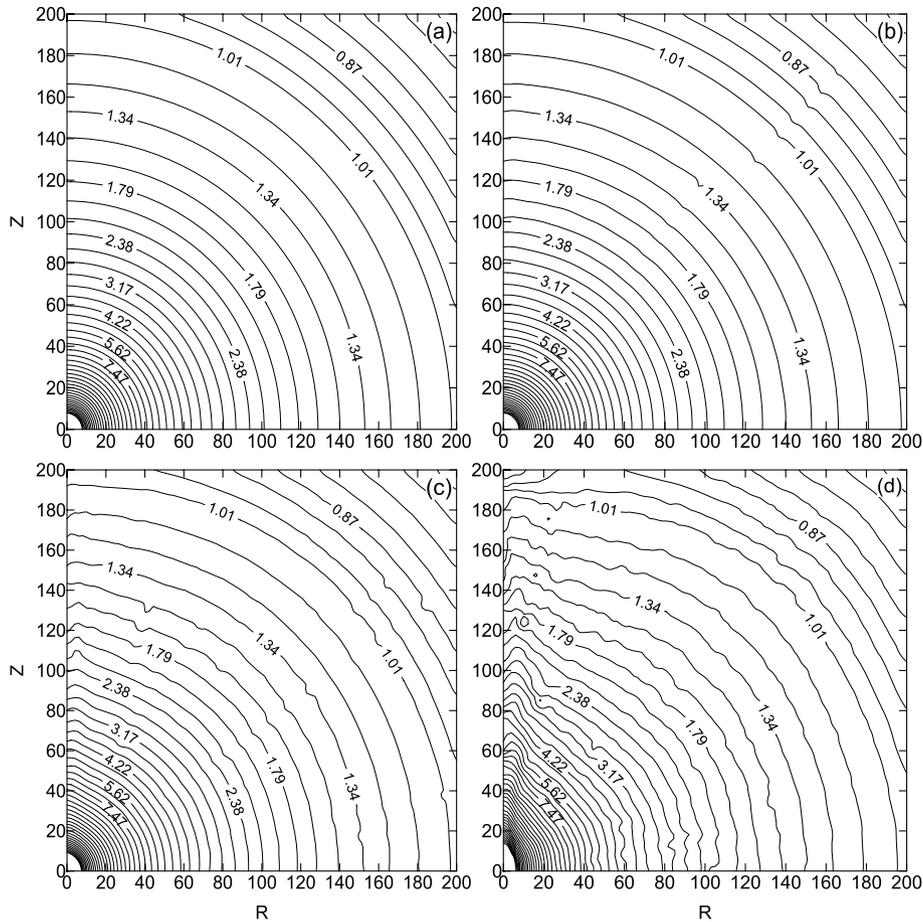
Figure 3. Changes in the density distribution in presence of cooling. $\lambda = 0$ and $\dot{m}_h = 1$ for all the cases. Disc accretion rate $\dot{m}_d$ used is (a) 1, (b) 2, (c) 5 and (d) 10, respectively [cases 1(a–d) of Table 1]. The density contours are drawn using the same contour levels as in Fig. 2(a).

multicolour blackbody spectrum supplied by the Keplerian disc is shown (solid line). The dotted, dashed, dash–dotted, double dot–dashed and double dash–dotted curves show the spectra for $\dot{m}_h = 0.5, 1, 2, 5$ and 10, respectively. The injected multicolour blackbody spectrum supplied by the Keplerian disc is shown (solid line). The spectrum becomes harder for higher values of $\dot{m}_h = 1$ as it is difficult to cool a higher density matter with the same number of injected soft photon. In Fig. 6(b), we show the directional dependence of the spectrum for $\lambda = 0$, $\dot{m}_h = 2$, $\dot{m}_d = 1$ (case 1f). The solid, dotted and dashed curves are for observing angles (a) 2°, (b) 45° and (c) 90°, respectively. All the angles are measured with respect to the rotation axis (z-axis). As expected, the photons arriving along the z-axis would be dominated by the soft photons from the Keplerian disc while the power-law would dominate the spectrum coming edge-on.

We now study the dependence of spectrum on the time delay between the injected photon and the outgoing photon. Depending on the number of scatterings suffered and the length of path travelled, different photons spend different times inside the Compton cloud. The energy gain or loss by any photon depends on this time. Fig. 6(c) shows the spectrum of the photons suffering different number of scatterings inside the cloud. Here, 1, 2, 3, 4, 5 and 6 show the spectrum for six different ranges of number of scatterings. Plot 1 shows the spectrum of the photons that have escaped from the cloud without suffering any scattering. This spectrum is nearly the same as the injected spectrum, only difference is that it is Doppler-shifted. As the number of scattering increases (spectrum 2, 3 and

4), the photons are more and more energized via inverse-Compton scattering with the hot electron cloud. For scatterings more than 19, the high-energy photons start losing energy through Compton scattering with the relatively lower energy electrons. Components 5 and 6 show the spectra of the photons suffering 19–28 scatterings and the photons suffering more than 28, respectively. Here the flow parameters are $\dot{m}_d = 1$, $\dot{m}_h = 10$ and $\lambda = 0$ (case 1h, Table 1).

In Fig. 6(d), we plot the spectrum emerging out of the electron cloud at four different time ranges. In the simulation, the photons take 0.01–130 ms to come out of the system. We divide this time range into four suitable bins and plot their spectra. Case 1h of Table 1 is considered. We observe that the spectral slopes and intensities of the four spectra are different. As the photons spend more and more time inside the cloud, the spectrum gets harder (plots 1, 2 and 3). However, very high energy photons which spend maximum time inside the cloud lose some energy to the relatively cooler electrons before escaping from the cloud. Thus the spectrum 4 is actually the spectrum of Comptonized photons.

4.2 Compton cloud with very low angular momentum

We now turn our attention to the case where the cloud is formed by a low angular momentum flow. In this case, the flow is already axisymmetric and due to centrifugal force a weak shock wave or at least a density wave would be formed. In Figs 7(a–b), we show the contours of constant density [Fig. 7(a)] and temperature [Fig. 7(b)] when no radiative transfer is included. Here the specific angular
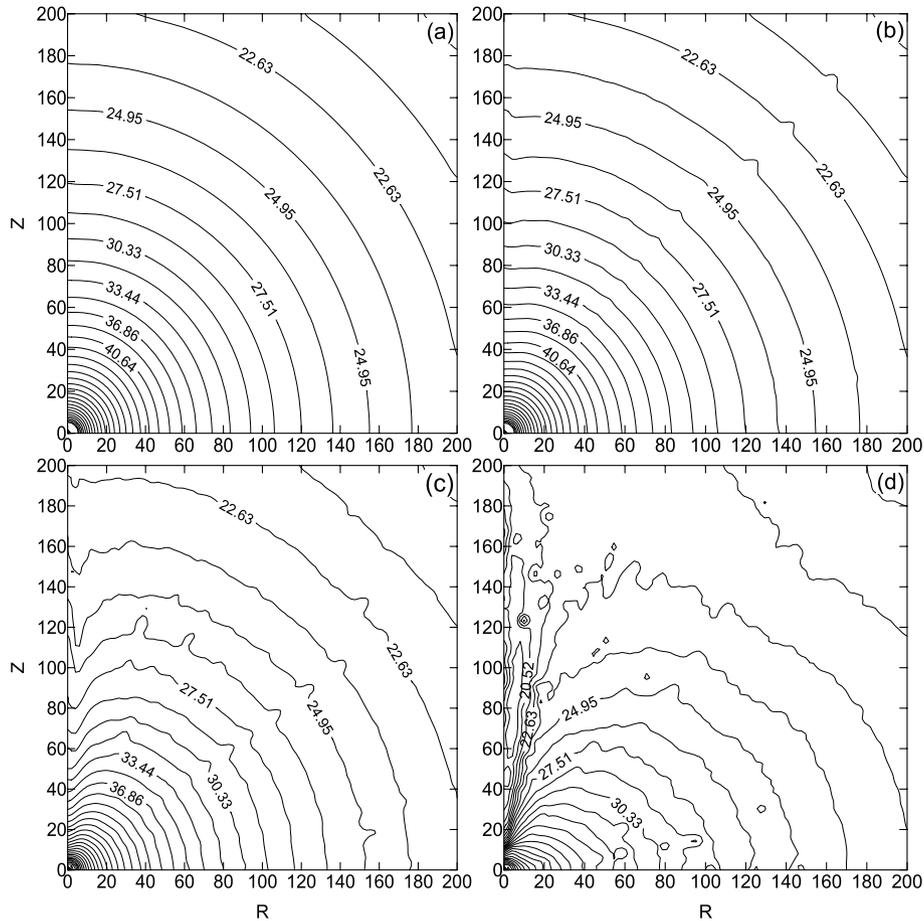
Figure 4. Changes in the temperature distribution in presence of cooling. $\lambda = 0$ and $\dot{m}_h = 1$ for all the cases. Disc accretion rate $\dot{m}_d$ used is (a) 1, (b) 2, (c) 5 and (d) 10, respectively [cases 1(a–d) of Table 1]. Contours are drawn using the same levels as in Fig. 2(b).

momentum of $\lambda = 1$ was chosen. Density contour levels are drawn from 0.001–55.35 (the successive level ratio is 1.5) and 55.35–73.73 (successive level ratio is 1.1). Temperature contour levels are drawn from 2.3–11.64 (successive level ratio is 1.5) and 11.64–64.71 (successive level ratio is 1.1). We note that a shock has been formed which bends outwards away from the equatorial plane (Ryu et al. 1997; Giri et al. 2010.). In Figs 8(a–d), we show results of inserting a Keplerian disc in the equatorial plane. The inner edge is located at $3r_g$, the marginally stable orbit. Here, $\dot{m}_h = 1$ and $\dot{m}_d =$ (a) 1, (b) 2, (c) 5 and (d) 10, respectively [cases 2(a–d) of Table 1]. The densities used to draw the contours are the same as that in Fig. 7(a). As the Keplerian disc rate is increased, the intensity of the soft photons interacting with the high optical depth (post-shock) region is increased. In Fig. 8(d), we observe that the conical region around the axis is considerably cooler. Thus, the density around the shock is enhanced. However, most importantly, with the increase in disc accretion rate, i.e. cooling, the shock location moves in closer to the black hole. This result has been already shown in the context of the bremsstrahlung cooling (Molteni et al. 1996). In Figs 9(a–d), we present the corresponding temperatures. The parameters are the same as in Figs 8(a–d) and the temperatures used to draw the contours are the same as that in Fig. 7(b). The Comptonization in the shocked region cools it down considerably. Otherwise, not enough visible changes in the thermodynamic variables are seen. To understand the detailed effects of the radiative transfer on the dynamics of the flow, we take the differences in the pressure and velocity at each

grid point of the flow for cases 1d and 2d of Table 1. In Figs 10(a–b), we show the difference between the results of a purely hydrodynamical flow and the results by taking the Comptonization into account. Fig. 10(a) is for the flow with no angular momentum, and Fig. 10(b) is drawn for the specific angular momentum $\lambda = 1$. The contours are of constant $\Delta P = P_c - P_a$, where P is the pressure and the subscripts 'c' and 'a' represent the pressure with and without cooling, respectively. The arrows represent the difference in velocity vectors in each grid. As expected, in both the cases, the changes are maximum near the axis. The fractional changes in pressures and velocities are anywhere between ~ 0 (outer edge) and ~ 25 per cent (inner edge and near the axis). Because of shifts of the shock location towards the axis, the variation of the velocity is also highest in the vicinity of the shock. Most importantly, the matter starts to fall back after losing the outward drive. This is the Chakrabarti & Manickam (2000) mechanism which is believed to decide the nature of the light curves of objects containing outflows. Thus we prove that not only the symmetry is lost by the insertion of an axisymmetric soft-photon source, but the cooling process also plays a major role in deciding the dynamics of the flow.

We now turn our attention to the dynamical variables and spectral behaviour of the rotating flow. In Fig. 11(a), we show the variation of the average temperature of the Compton cloud as a function of the iteration time of the coupled code [cases 2(a–d), Table 1]. With the increase in the disc rate, the temperature of the Compton cloud saturates at a lower temperature. Fig. 11(b) shows the effect of the
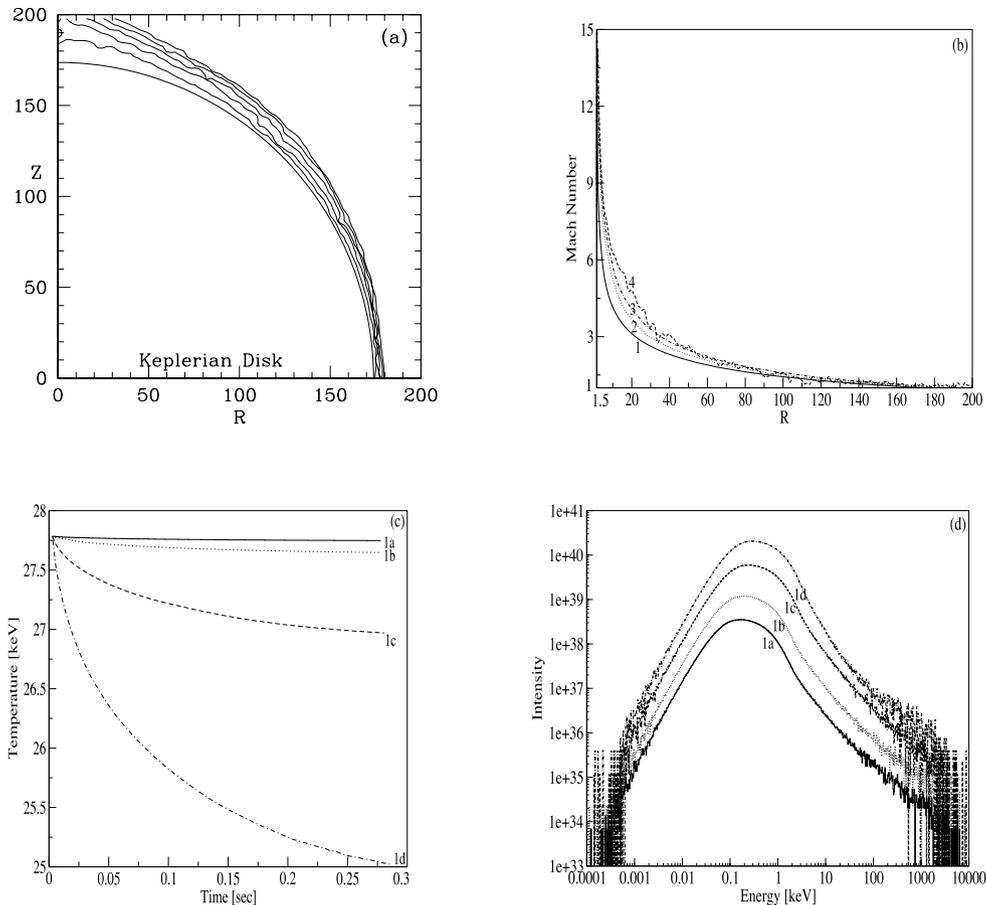
Figure 5. (a) Sonic surfaces at different stages of iterations. The final curve represents the converged solution. The initial spherical sonic surface becomes prolate spheroid due to cooling by the Keplerian disc at the equatorial plane. Parameters are for case 1d (Table 1). (b) Mach number variation as a function of distance after a complete solution of the radiative flow is obtained. Plot 1 corresponds to the solution from adiabatic Bondi flow. Plots 2–4 are the solutions along the equatorial plane, the diagonal and the axis of the disc. Parameters are for case 1d (Table 1). (c) Variation of the average temperature of the Compton cloud as the iteration proceeds when the disc accretion rate is varied, $\dot{m}_h = 1$. The solid, dotted, dashed and dot–dashed plots are for $\dot{m}_d = 1, 2, 5$ and 10, respectively. Case numbers (Table 1) are marked. With the increase of disc rate, the temperature of the Compton cloud converges to a lower temperature. (d) Variation of the spectrum with the increase of disc accretion rate. Parameters are the same as in (c). With the increase in $\dot{m}_d$, the intensity of the spectrum increases due to the increase in N_{inj} (see Table 1). The spectrum is softer for the higher value of $\dot{m}_d$. Spectral slopes for each of these spectra are listed in Table 1.

decrease in cloud temperature on the spectrum due to the increase in disc rate. As we increase the disc rate, keeping the halo rate fixed, the spectrum becomes softer.

In Fig. 12, we show the effects of the increase of the electron number density (due to the increase of $\dot{m}_h$) for a fixed disc rate. The spectrum becomes harder as we increase the halo rate keeping the number of injected soft the photons the same.

We observe that the emerging spectrum has a bump, especially at higher accretion rates of the halo, at around 100 keV [e.g. the spectra marked 1g, 1h in Fig. 6(a) and the spectrum marked 2h in Fig. 12]. A detailed analysis of the emerging photons having energies between 50 to 150 keV was made to see where in the Compton cloud these photons were produced. In Fig. 13(a), we present the number of scatterings inside different spherical shells within the electron cloud suffered by these photons ($50 < E < 150$ keV) before leaving the cloud. Parameters used are $\dot{m}_d = 1$, $\dot{m}_h = 10$ and $\lambda = 0$. The light and dark shaded histograms are for the cloud with and without bulk velocity components, respectively. We find that the presence of bulk motion of the infalling electrons pushes the photons towards the hotter and denser [Figs 2(a–b)] inner region of the cloud to suffer more and more scatterings. We find that the photons responsible for

the bump suffered maximum number of scatterings around $8r_g$. From the temperature contours, we find that the cloud temperature around $8r_g$ is $\sim$100 keV. This explains the existence of the bump. In Fig. 13(b), we consider all the outgoing photons independent of their energies. The difference between the two cases is not so visible. This shows that the bulk velocity contributes significantly to produce the highest energy photons.

In Fig. 14, we explicitly showed the effects of the bulk velocity on the spectrum. We note that the bump disappears when the bulk velocity of the electron cloud is chosen to be zero (curve marked 2). This fact shows that the region around $8r_g$ in presence of the bulk motion behaves more like a blackbody emitter, which creates the bump in the spectrum. Since the photons are suffering large number of scatterings near this region ($8r_g$), most of them emerge from the cloud with the characteristic temperature of the region. The effect of bulk velocity in this region is to force the photons to suffer larger number of scatterings. This bump vanishes for lower density cloud (low $\dot{m}_h$) as the photons suffer lesser number of scatterings. The photons which are scattered close to the black hole horizon and escape without any further scattering produce the high-energy tail in the output spectrum. Curve 3 of Fig. 14 shows the intensity
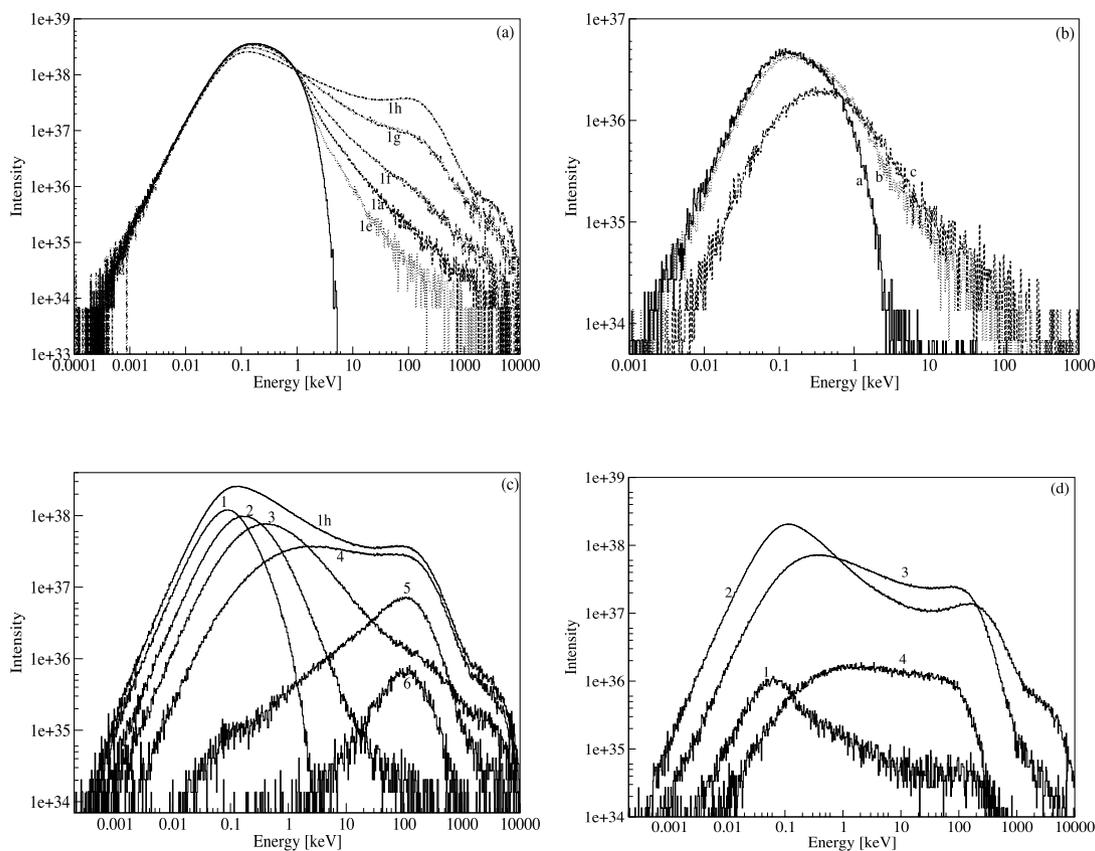
Figure 6. (a) Variation of the spectrum with the increase of the halo accretion rate, keeping the disc rate ($\dot{m}_d = 1$) and angular momentum of the flow ($\lambda = 0$) fixed. The dotted, dashed, dash–dotted, double dot–dashed and double dash–dotted curves show the spectra for $\dot{m}_h = 0.5, 1, 2, 5$ and 10, respectively. The injected multicolour blackbody spectrum supplied by the Keplerian disc is shown (solid line). (b) Directional dependence of the spectrum: $\lambda = 0$, $\dot{m}_h = 2$ and $\dot{m}_d = 1$ are the flow parameters. The solid, dotted and dashed curves are for observing angles $2°$, $45°$ and $90°$, respectively. All the angles are measured with respect to the rotation axis (z-axis). Intensity of spectra emerging from the cloud after suffering various number of scatterings (c) and at four different times (d) immediately after the injection of soft photons. Case 1h is assumed. The spectra of the photons suffering 0, 1–2, 3–6, 7–18, 19–28 and more than 29 scatterings are shown by the plots 1, 2, 3, 4, 5 and 6 [Fig. 6(c)] respectively, within the cloud. Curve 1h is the net spectrum for which these components are drawn. As the number of scattering increases, the photons gain more and more energy from the hot electron cloud through inverse-Comptonization process. The spectra of the photons spending 0.01–1, 1–40, 40–100 and more than 100 ms time inside the electron cloud are marked by 1, 2, 3 and 4 [Fig. 6(d)], respectively.

spectrum of case 1h (Table 1), when there are zero bulk velocity inside $3r_g$. We find that in the absence of bulk velocity inside $3r_g$, the high-energy tail in the curve 1h vanishes. This is thus a clear signature of the presence of bulk motion Comptonization near the black hole horizon.

5 SUMMARY AND DISCUSSIONS

In this paper, we have extended our previous work using Monte Carlo simulations (Ghosh, Chakrabarti & Laurent 2009; Ghosh et al. 2010) to include the effects of Comptonization on the dynamics of the accreting halo having zero and very low angular momentum. We studied the properties of the emerging spectrum from the Chakrabarti–Titarchuk model of a two-component flow, one component being the Keplerian disc on the equatorial plane and the other component is the low angular momentum accreting halo, which is acting as the Compton cloud. In Table 1, we have given the parameters of all the cases which were run. We note that as we enhance $\dot{m}_d$, N_{inj} ($\sim \dot{m}_d^{3/4}$; see Section 2.2) is also enhanced, increasing the number of photons N_{sc} undergoing Compton scattering. If we keep the halo rate $\dot{m}_h$ fixed, then increasing $\dot{m}_d$ increases N_{unsc}, the number of photons escaping from the disc while keeping p almost unchanged. For cases 1(a–d) and 2(a–d), the percentage of

photons undergoing scattering p is ~ 20 and ~ 19 per cent, respectively. When we increase $\dot{m}_h$, keeping $\dot{m}_d$ constant, this percentage increases rapidly due to the decrease in N_{unsc}. We see from Table 1, as $\dot{m}_h$ is increased from 0.5 to 10, keeping $\dot{m}_d = 1$ [cases 1e, 1a, 1(f–h)], percentage of scattered photon increases from ~ 11 to ~ 76 per cent. The same situation prevails for the $\lambda = 1$ cases [cases 2e, 2d, 2(f–h)], where p increases from ~ 11 to ~ 51 per cent, for the increase in $\dot{m}_h$ from 0.5 to 5, keeping $\dot{m}_d = 10$. N_{bh} remains almost constant if we keep the halo rate constant. If we increase the halo rate, N_{bh} increases rapidly, because increase in $\dot{m}_h$ increases the density of the cloud and thus pushes the photons towards the black hole. As we increase $\dot{m}_d$, the cooling time t_0 decreases, since with the increase of $\dot{m}_d$ number of soft photon increases. Thus, the cloud cools down at a faster rate. We also note that t_0 decreases as $\dot{m}_h$ increases, due to the increase of N_{sc}. Spectral index α increases with the disc rate for a fixed halo rate, and it decreases with halo rate for a fixed $\dot{m}_d$. This can be explained by the fact that as we increase $\dot{m}_d$, the electron cloud becomes cooler, the spectrum gets softened. On the other hand, when we increase the number of hot electron inside the cloud (i.e. $\dot{m}_h$), for the same N_{inj} we get a hotter system. This makes the spectrum harder. These results are consistent with the Chakrabarti–Titarchuk scenario of two-component accretion.
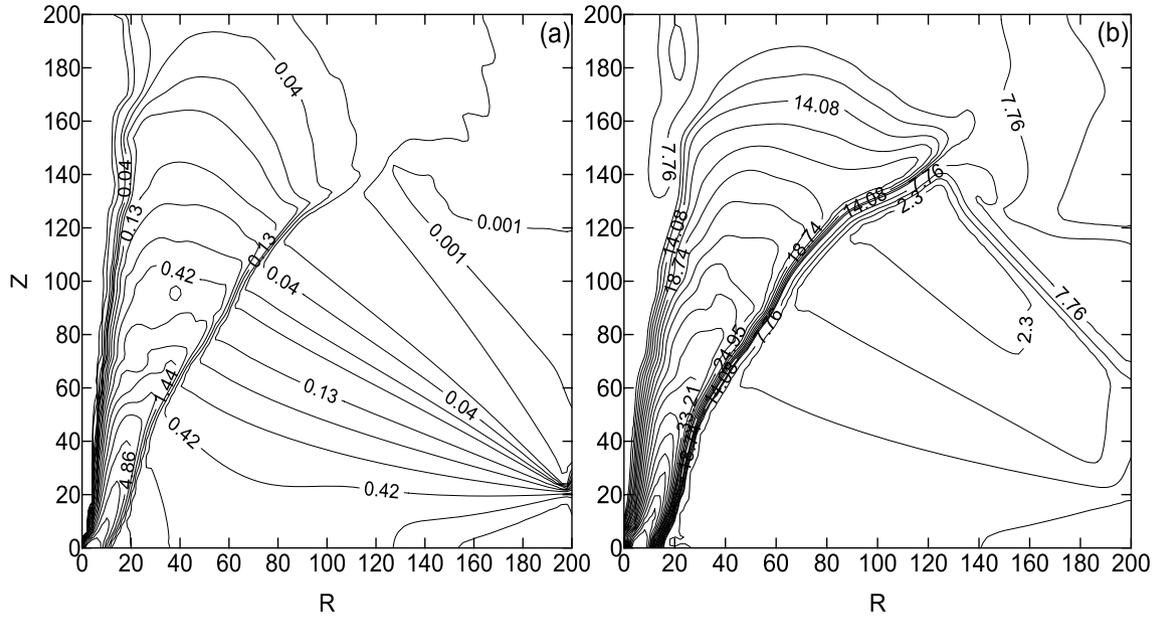
Figure 7. Density (a) and temperature (b) contours inside the halo ($\lambda = 1$) in the absence of Compton cooling. Densities are in normalized unit and temperatures are in keV. See text for details.
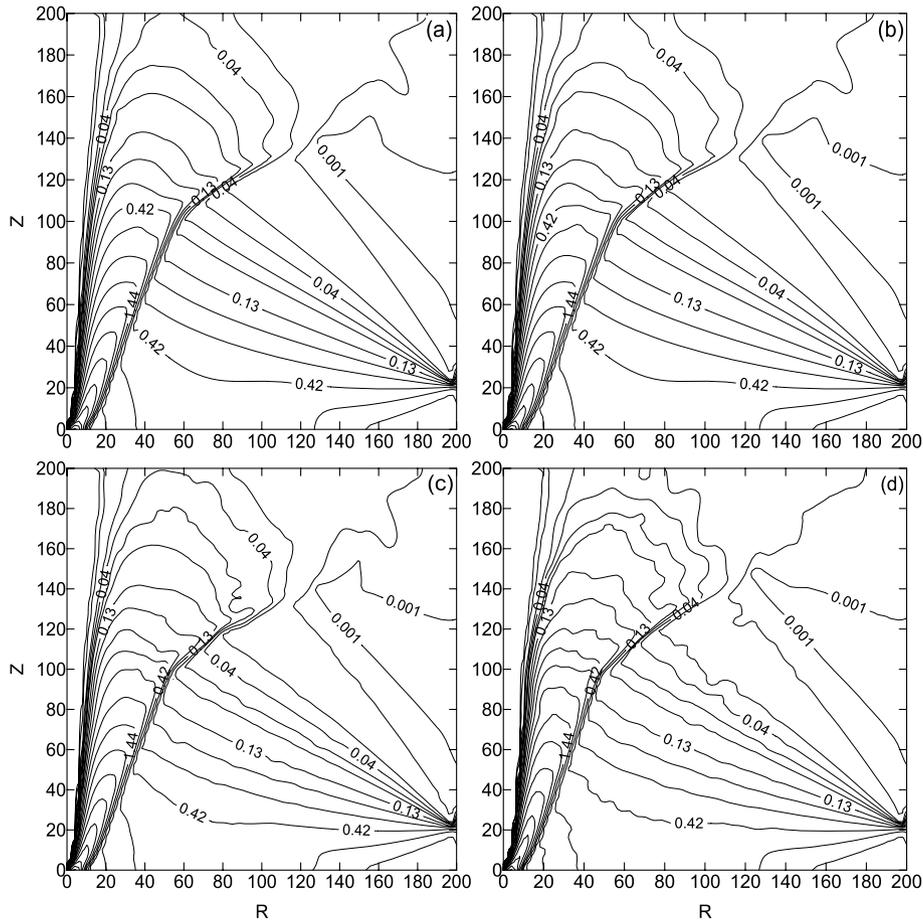
Figure 8. Change in the density contours in presence of cooling ($\lambda = 1$) (see text for details). The conical region between the axis and shock wave becomes denser as the accretion rate of the Keplerian disc is increased.
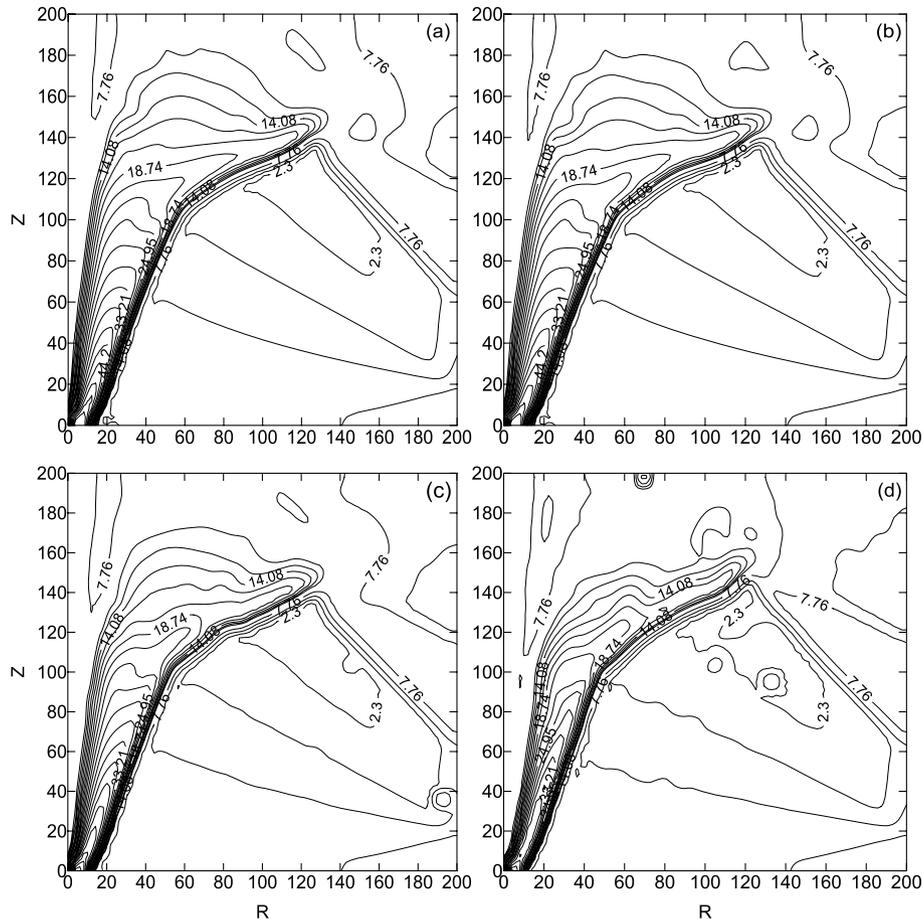
Figure 9. Change in the temperature contours in presence of cooling. The parameters are the same as in Figs 8(a–d). The temperature values used to draw the contours are the same as in Fig. 7(b). Note that the shock shifts closer to the axis with the increase in disc accretion rate.
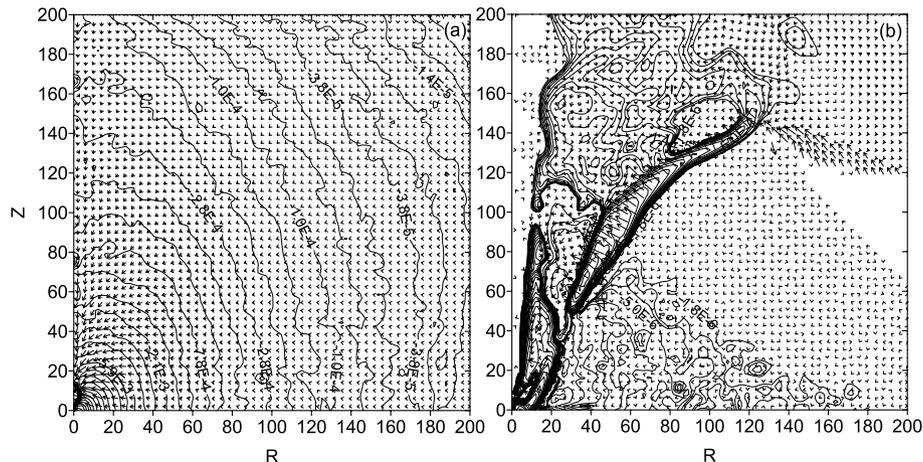
Figure 10. Difference in pressure and velocities between the flow with Comptonization and without Comptonization. Other parameters remain exactly the same. The cases are (a) case 1d and (b) case 2d of Table 1, respectively.

Our major conclusions are the followings.

(i) In the presence of an axisymmetric disc which supplies soft photons to the Compton cloud, even an originally spherically symmetric accreting Compton cloud becomes axisymmetric. This is because, due to the higher optical depth, there is a significant cooling near the axis of the intervening accreting halo between the disc and the axis.

(ii) Due to the cooling effects close to the axis, the pressure drops significantly, which may change the flow velocity up to 25 per cent. This effect becomes more for low angular momentum flows which produce shock waves close to the axis. The post-shock region cools down and the outflow falls back to the disc. This shows that the Chakrabarti & Manickam (2000) mechanism of the effects of Comptonization on outflows does take place.
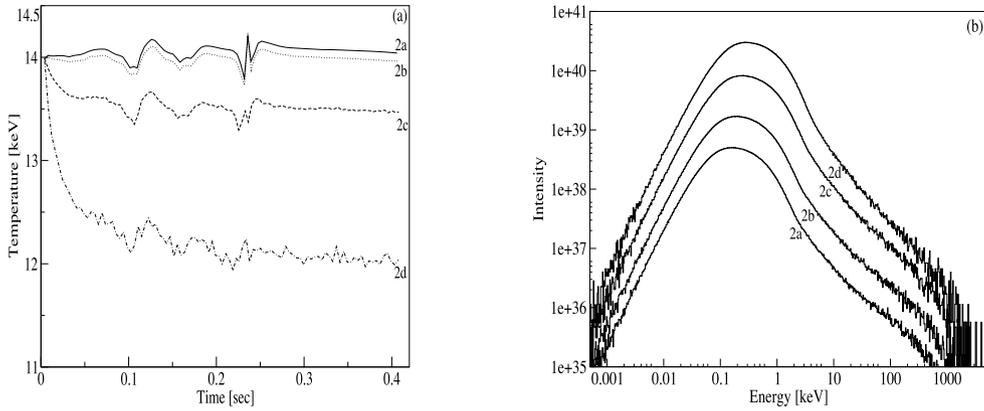
Figure 11. Variation of (a) average temperature of the Compton cloud with iteration time and (b) spectrum with the increase of disc accretion rate. $\lambda = 1$ and $\dot{m}_h = 1$ are used. The solid, dotted, dashed and dash–dotted plots are for $\dot{m}_d = 1, 2, 5$ and 10, respectively. With the increase in the disc rate, the temperature of the Compton cloud saturates at lower temperature. The solid, dotted, dashed and dash–dotted curves show the spectrum for $\dot{m}_d = 1, 2, 5$ and 10, respectively. The spectrum is softer for higher value of $\dot{m}_d$.
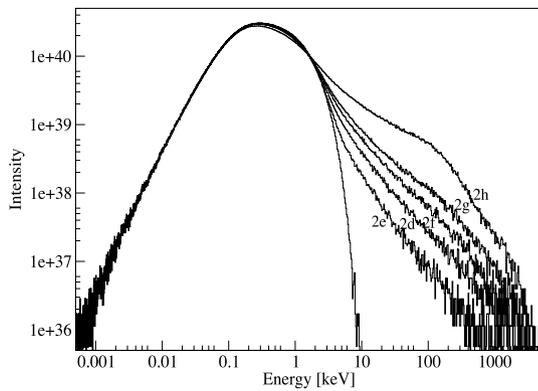
Figure 12. Variation of the spectrum with the increase of the halo accretion rate, keeping the disc rate ($\dot{m}_d = 10$) and angular momentum of the flow ($\lambda = 1$) fixed. The case number for which a spectrum is drawn is marked on it. The unmarked plot is the injected spectrum. The resulting spectrum becomes harder for the higher values of $\dot{m}_h$.
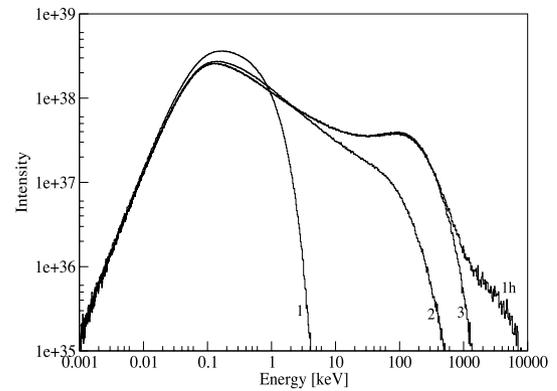
Figure 14. The spectrum for the case 1h. The curves marked 2 and 3 give the spectra when the bulk velocity of the electron is absent for the whole cloud and for the cloud inside $3r_g$, respectively. The curve marked 1 gives the injected spectrum. The bulk motion Comptonization of the photons inside the $3r_g$ radius creates the hard tail. The bump near $100\,\mathrm{keV}$ is a combined effect of the temperature and bulk velocity of the rest of the cloud.
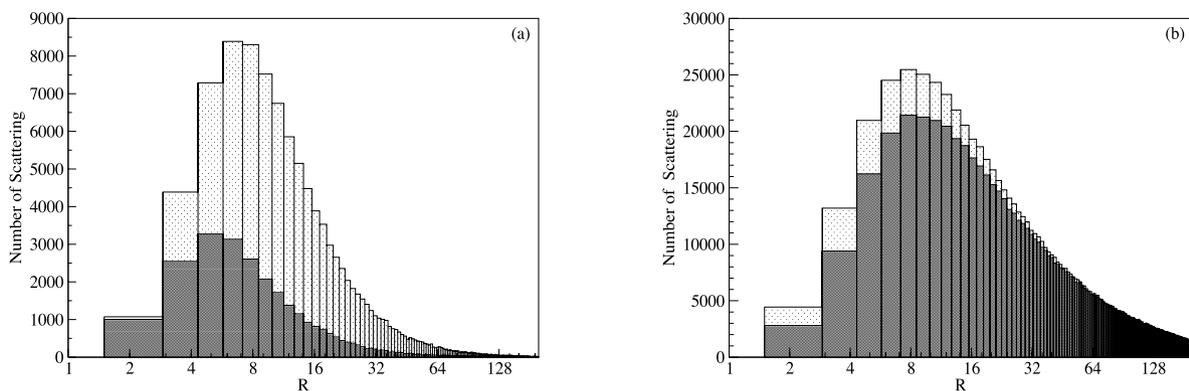
Figure 13. Number of scatterings inside the spherical shell between R to $R + \delta R$ ($\delta R \sim 1.4$). The light and dark shaded histograms are for the cloud with and without bulk velocity, respectively. (a) Only the photons emerging from the cloud with energies E, where $50\,\mathrm{keV} < E < 150\,\mathrm{keV}$, are considered here. (b) All the photons emerging from the cloud are considered here. Parameters used: $\dot{m}_d = 1$, $\dot{m}_h = 10$ and $\lambda = 0$.

(iii) The emitted spectrum is direction-dependent. The spectrum along the axis shows a large soft bump, while the spectrum along the equatorial plane is harder.

(iv) Photons which spend more time (up to 100 ms in the case considered) inside the Compton cloud produce harder spectrum as they scatter more. However, if they spend too much (above 100 ms) time, they transfer their energies back to the cooler electrons while escaping. These results would be valuable for interpreting the timing properties of the radiation from black hole candidates.

ACKNOWLEDGMENTS

REFERENCES

Chakrabarti S. K., 1989, ApJ, 347, 365
Chakrabarti S. K., 1990, Theory of Transonic Astrophysical Flows. World Scientific, Singapore
Chakrabarti S. K., 1996, Phys. Rep., 266, 229
Chakrabarti S. K., Manickam S. G., 2000, ApJ, 531, L41
Chakrabarti S. K., Titarchuk L. G., 1995, ApJ, 455, 623
Chakrabarti S. K., Acharyya K., Molteni D., 2004, A&A, 421, 1
Coppi P. S., 1992, MNRAS, 258, 657
Dutta B. G., Chakrabarti S. K., 2010, MNRAS, 404, 2136
Ghosh H., Chakrabarti S. K., Laurent P., 2009, Int. J. Modern Phys. D, 18, 1693
Ghosh H., Garain S. K., Chakrabarti S. K., Laurent P., 2010, Int. J. Modern Phys. D, 19, 607
Giri K., Chakrabarti S. K., Samanta M. M., Ryu D., 2010, MNRAS, 403, 516
Haardt F., Maraschi L., 1993, ApJ, 413, 507
Janiuk A., Czerny B., 2000, New Astron., 5, 7
Kobayashi Y., Kubota A., Nakazawa K., Takahashi T., Makishima K., 2003, PASJ, 55, 273
Lyubarskii Y. E., 1997, MNRAS, 292, 679
Merloni A., Fabian A. C., 2001, MNRAS, 321, 549
Molteni D., Sponholz H., Chakrabarti S. K., 1996, ApJ, 457, 805
Molteni D., Toth G., Kuznetsov O. A., 1999, ApJ, 516, 411
Paczyński B., Wiita P. J., 1980, A&A, 88, 23
Pottschmidt K., Chernyakova M., Zdziarski A. A., Lubinski P., Smith D. M., Bezayiff N., 2006, A&A, 452, 285
Proga D., 2007, ApJ, 661, 693
Proga D., Ostriker J. P., Kurosawa R., 2008, ApJ, 676, 101
Ryu D., Chakrabarti S. K., Molteni D., 1997, ApJ, 474, 378
Shakura N. I., Sunyaev R. A., 1973, A&A, 24, 337 (SS73)
Smith D. M., Heindl W. A., Swank J. H., 2002, ApJ, 569, 362
Soria R., Wu K., Hannikainen D., McCollough M., Hunstead R., 2001, in Yaqoob T., Krolik J. H., eds, Proc. JHU/LHEA Workshop on X-ray Emission from Accretion on to Black Holes, Baltimore, p. 65, preprint (astro-ph/0108084v1)
Sunyaev R. A., Titarchuk L. G., 1980, ApJ, 86, 121
Titarchuk L. G., Lyubarskij Y., 1995, ApJ, 450, 876
Wandel A., Liang E. P., 1991, ApJ, 380, 84
Wu K. et al., 2002, ApJ, 565, 1161
Zdziarski A. A., Lubinski P., Gilfanov M., Revnitsev M., 2003, MNRAS, 342, 355

This paper has been typeset from a TeX/LaTeX file prepared by the author.